PROCEEDINGS A

royalsocietypublishing.org/journal/rspa

Research

Cite this article: Yang Y, Billingham J, Axinte D, Liao Z. 2023 A rational approach to beam path planning in additive manufacturing: the inverse heat placement problem. *Proc. R. Soc. A* **479**: 20220386.
https://doi.org/10.1098/rspa.2022.0386

Received: 5 June 2022
Accepted: 22 December 2022

Subject Areas:
mathematical modelling, materials science, thermodynamics

Keywords:
additive manufacturing, *Inverse Heat Placement Problem*, uniform microstructure property

Author for correspondence:
Zhirong Liao
e-mail: zhirong.liao@nottingham.ac.uk

THE ROYAL SOCIETY
PUBLISHING

A rational approach to beam path planning in additive manufacturing: the inverse heat placement problem

Yue Yang[1], John Billingham[2], Dragos Axinte[1] and Zhirong Liao[1]

[1]Machining and Condition Monitoring Group, Faculty of Engineering, and [2]School of Mathematical Sciences, Faculty of Science, University of Nottingham, Nottingham NG7 2RD, UK

JB, 0000-0002-4392-5770; DA, 0000-0002-3595-0933;
ZL , 0000-0002-7026-9027

High demand for components with complex geometries at macro and micro levels drives the development of additive manufacturing (AM). However, the scientific basis for designing energy beam scanning strategies (e.g. beam scanning speed, beam path, beam power) still relies on trial and error approaches (i.e. experimental/simulation of predefined beam trajectories) followed by the evaluation of process outcomes (e.g. structural/metallurgical properties of the built parts); this is the Direct Problem. To address such drawbacks, this paper reports, for the first time, a mathematical model for selecting key parameters related to beam exposure time in AM processes as an attempt to improve the build part's uniform properties, i.e. the *Inverse Heat Placement Problem*. Our algorithm yields variable beam scanning speeds and optimized beam paths for achieving a desired maximum temperature distribution (uniform or target pattern) and is suitable for different circumstances and scanning strategies dependent on the print part configuration. Here, raster and spiral predefined beam paths are chosen as examples. Variable beam scanning speeds and optimized beam paths obtained from our algorithm are able to induce a desirable uniform maximum temperature distribution compared with the conventional approach of constant beam scanning speeds and a predefined beam path.

1. Introduction

Additive manufacturing (AM) is an enabling technology that can be used to print parts with complex three-dimensional shapes and structures for use in a broad range of industries. A wide variety of AM technologies exists, and many of them rely on an energy (laser, electron) beam to deliver localized heat to the growing part, which melts or sinters the material powder/wire in a layer-by-layer manner [1,2]. There have been many in-depth studies of the detailed mechanisms of AM processes, with focus ranging from the resulting microstructure [3–6] to large structural aspects such as geometrical distortion [7–9]. Theoretical studies mainly rely on computationally expensive, multi-physics packages (e.g. COMSOL, ALE3D) to simulate fine details of the small-scale phenomena (including melt pool geometry, and mushy zone solidification) that occur during AM processes and from these a selection of the 'optimal' working parameters for desired built part properties is made [10–12]. This is a 'direct' approach to the problem. Sets of operating parameters are selected first, and then the process outcomes (e.g. distribution of temperature in the powder bed) could be estimated by running off-the-shelf packages. If these outcomes are not as expected (usually the case in the first round of simulations), the procedure will be repeated until a near-optimal solution is obtained. This is time-consuming (as these multi-scale Multiphysics models are computationally expensive) but still can be considered a computational trial and error approach.

As a time-dependent process, AM mostly relies on the movement of an energy beam across the feature to be generated. This means that thermal energy is adaptively deposited into complex parts, which significantly affects process outcomes. Build quality and material properties have been shown to be highly dependent on processing parameters (e.g. beam power, scanning speed, track overlapping, etc.) [13,14]. Some studies consider the effect of the processing parameters by defining them as the input energy density, which is directly proportional to beam (most commonly laser) power but inversely proportional to scanning speed, hatching space and layer thickness [15–17]. This is a simplifying approach since these studies do not explicitly consider the influence of beam exposure time on their results. The beam exposure time means the period of time on which a given point is exposed to the energy beam. Under the Continuous Wave laser mode of operation in the AM system, the beam exposure time is controlled by the beam scanning speed. Moreover, the input energy density cannot fully characterize the complex interactions between printing outcomes and parameters. This is because even with constant input energy density, energy absorption varies notably when laser power and speed are changed [18,19]. This was validated by imaging the melt pool in a laser powder bed fusion process using an *in situ*, high-speed, high-energy X-ray imaging system [18,20,21].

Apart from these parameters, the scanning strategy defined by the path of the energy beam is also a decisive factor in establishing the required process outcomes. The most common approaches are to make the energy beam follow a raster path in straight lines under constant processing (e.g. scanning speed) parameters [22,23]; this approach neglects the influence of the varying beam dwell time at the end of the lines with the inherent influence of the amount of induced heat. These raster strategies at different alternating angles between the built layers, e.g. alternating with 45°, 67° and 90° rotation [24–26], are widely employed to improve the structural uniformity of the parts. It was found that the smaller re-melting area under 90° induces a smaller cooling rate and a smaller order of grain size in laser powder bed fusion copper alloys, generating a weak order of texture strength [27]. For 316 l stainless steel, the 30° angle shows better mechanical properties [28], and ±45° raster angle specimens exhibits a more ductile behaviour than 0° and 90° specimens [29].

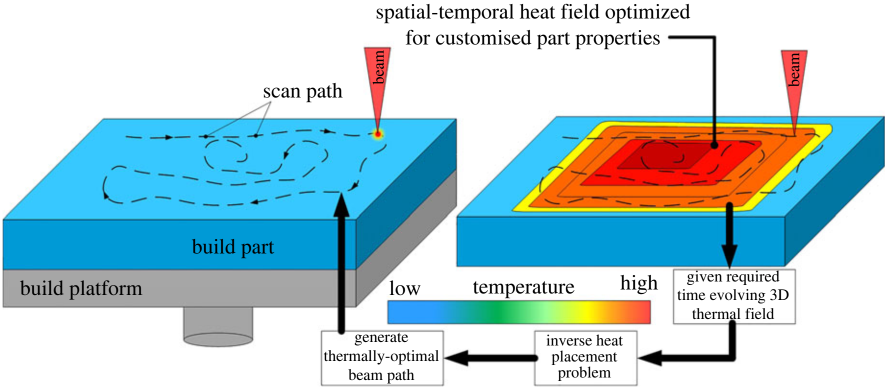

Figure 1. The *Inverse Heat Placement Problem* in AM processing.

Although this previous work makes a valuable contribution to understanding AM processes, there are few studies on how best to manage the dynamics of the thermal field in evolving parts. Some work on beam scanning strategy 'optimization' is implemented by printing numerous samples using different sets of parameters (sometimes using the design of experiments approach), and then observing the resulting grain size and crystallographic texture [30–32]. These 'optimal' scanning strategies are limited by the predefined process conditions and should be thought of as *ad hoc* 'optima' obtained by solving only the direct or forward problem.

The pivotal question here is: Why has the usual approach been to use raster paths, considering that the inherent acceleration of the energy beam at the end of the raster paths (inducing varying exposure times) will automatically induce different amounts of energies along the beam paths, which results in non-homogeneous AM built structures? Of course, someone can choose other beam paths (e.g. spiral [33], Hilbert [23]), but still, there are no in-depth (i.e. physics-based) reasons for choosing these beam path strategies. Ultimately, it can be chosen to be any arbitrary/predefined beam path, but what is the scientific basis for doing so? Apart from beam paths, beam scanning speed, beam power, beam size, hatching space and layer thickness also affect the heat placement in AM. The heat placement is related to general challenges in AM, in terms of thermal stress reduction and surface quality improvement. Some thermal stress prediction models were proposed to obtain the relationship between controlling parameters and thermal stress [34,35]. To reduce it, combined laser beams were used to generate post-heating to avoid an extremely high temperature gradient [36]. The investigations on surface quality concerning the controlling parameters in AM are normally experimental based [37–39].

In the authors' opinion, this still could be considered a trial-and-error approach and, as will be demonstrated later in the paper, these arbitrarily selected controlling parameters result in highly variable heat-induced fields in the AM built structure.

We believe that what really needs to be addressed is the *Inverse Heat Placement Problem*, i.e. given bounds on the temperature and its temporal and spatial gradients (needed to control process outcomes), determine a suitable beam path (position and speed) and set of other process parameters (figure 1). Some partial attempts have been made to solve this problem. Farshidianfar *et al*. [40] developed a closed-loop direct energy deposition system by employing an IR thermography camera to monitor the real-time cooling rate which is set as the reference for adjustments of the scanning speed in real-time, aiming to improve the uniformity of the microstructure and hardness. Similar work is implemented by Rezaeifar & Elbestawi [41] on porosity mitigation by using a PID controller to adjust laser power based on the measurement from the thermal camera and IR-transmissive window; however, no modelling work has been undertaken here and therefore, the route to address it is by using an additional monitoring system to enable corrections of parameters. Halsey *et al*. [42] showed theoretically how local microstructure can be controlled by manipulating the position of the electron beam spot (discontinuous heating) and dwell time on individual pixels that was optimized by a genetic algorithm to find the solution of the physics-based model.

However, it has been shown for other dwell-time energy beam processes (e.g. waterjet milling, pulsed laser ablation, focused ion beam) [43–46], that the solution to the *Inverse Heat Placement Problem* does not usually consist of simple linear paths and significant scientific, engineering and mathematical challenges must be dealt with to make progress.

The *Inverse Heat Placement Prob*lem in AM (i.e. laser powder bed) that we aim to solve here is to obtain uniform microstructure properties by controlling the beam scanning path and speed. From investigations of the solidification process, the microstructures of as-built parts in AM are dependent on thermal gradient and solidification rate which are influenced by the heat placement [47]. Due to the non-uniform distribution of beam energy and its spatial variations, thermal gradient and solidification rate vary in real-time from location to location in the mushy zone, as well as microstructure morphology and size variations. Controlling the starting point of the solidification processes makes it possible to improve the uniformity of the features of the built part. In other words, it is difficult to obtain constant and uniform thermal gradients and solidification rates across the whole three-dimensional workpiece if we do not address the *Inverse Heat Placement Problem*: given a required 'uniform' maximum temperature distribution on the part, determine the optimal (laser) beam path and scanning speed. This is the basis of our approach in this paper.

By contrast to previous work, we propose a generic theoretical modelling approach for the *Inverse Heat Placement Problem* in AM that in principle allows us to obtain uniform properties in AM built structures (e.g. microstructure, deformations, residual stresses). As we control the temperature distribution when building the AM structure, this model provides references for further customized intelligent microstructure design in AM and presents, as discussed later, the need for open-source control in three-dimensional printing machines that allows the implementation of such scientific-based (but very effective) beam path generators.

2. Theoretical modelling

In AM, the beam energy is normally considered as top-hat or Gaussian distribution [48]. In our case, the Gaussian distribution is accepted, i.e. with more energy at the centre than at the edge. The essence of processing parameter control is how to organize the motion of this centre-focused energy beam to obtain the desired outcomes. This is similar to other time-dependent material removal processes (abrasive waterjet milling, pulsed laser ablation, focus ion beam milling and shape adaptive grinding), but the difference is that the heat generated for melting the material powder in AM is not transported away immediately when the energy beam moves to another position; it gradually moves through the adjacent gas atmosphere and powder. Energy absorption, accumulation and dissipation in time underlies temperature evolution in the target region, which increases the complexity of the resulting microstructure.

Our aim in solving the *Inverse Heat Placement Problem* is to optimize the laser speed and path (with an example on laser powder bed AM) to obtain a close to constant maximum temperature in the laser powder bed fusion system. We consider here the target of our optimization as the maximum temperature on the surface, as an example and a good start to obtain uniform characteristics (e.g. microstructure, residual stresses) of the built structure, on the assumption that cooling rates are constant.

But before solving the *Inverse Heat Placement Problem* (given the maximum temperature in the structure, determine the beam path and scanning speed), we need to consider the direct problem. Therefore, we first use a transient thermal analysis of a half-space of uniform material with an insulated boundary to represent the print sample and thereby solve the *Inverse Heat Placement Problem* to obtain the time-dependent temperature distribution.

(a) Transient thermal analysis

The main focus of our work is to make a first attempt at optimizing the beam path to control material properties. With this in mind, we have chosen to use the simplest possible thermal model, namely one in which none of the thermal properties of the material is temperature-dependent. While this is of course not the case, it allows us to use a Green's function formulation, and consequently develop a very efficient numerical solution method for the *Inverse Heat Placement Problem*. As we shall see, this proof-of-concept solver indicates that it is indeed possible to improve on the usual constant speed raster paths for optimization of material properties. In subsequent work, a more realistic model could use a model with temperature-dependent material properties, for which more sophisticated methods for both the forward problem (finite difference or finite element) and the *Inverse Heat Placement Problem* (an adjoint problem solver) will be required.

The initial temperature is assumed constant (here, it is room temperature, 25°C). The evolution equation is [49]

$$\frac{\partial T}{\partial t} - \nabla.(\lambda \nabla T) = q(x, y, z, t), \quad t > 0,\ \boldsymbol{x} \in D, \tag{2.1}$$

where D is the domain containing the workpiece ($z \leq 0$); $T(\boldsymbol{x}, t)$ is the workpiece temperature at point (x, y, z) and $q(\boldsymbol{x}, t)$ is the source strength, which models the heat placed in the sample by the incident laser. This is to be solved subject to a no flux condition on the upper surface along with initial conditions $T(\boldsymbol{x}, 0) = \text{constant}$.

The heat supplied by the laser beam is modelled as Gaussian, with exponential decay in the z-direction, so that [45]:

$$q(x, y, z, t) = \left(\frac{\eta P}{\pi r_b^2}\right) \exp(-((x - x_b(t))^2 + (y - y_b(t))^2)/r_b^2) \exp(z/z_p)/z_p, \tag{2.2}$$

where η is the laser heat absorption ratio; P is the laser power; r_b is the laser spot radius; $(x_b(t), y_b(t))$ is the transient position of the laser spot centre on the upper surface, $z = 0$ and z_p is the penetration depth of the laser beam into the powder.

To solve the linear heat conduction equation (equation (2.1)), we use the Green's function (G), which is the solution when $q(x, y, z, t)$ is a delta function in space and time. This can be used to calculate the evolution of the temperature distribution for any heat flux $q(x, y, z, t)$, so that for $T(x, y, z, t)$ given by (equation (2.2)),

$$T(x, y, z, t) = \frac{\alpha}{k} \int_{\tau=0}^{t} \int_{x_q=-\infty}^{\infty} \int_{y_q=-\infty}^{\infty} \int_{z_q=-\infty}^{\infty} G(x, y, z, t|x', y', z', \tau) q(x', y', z', \tau)\, \mathrm{d}x' \mathrm{d}y' \mathrm{d}z' \mathrm{d}\tau, \tag{2.3}$$

with $G(x, y, z, t|x', y', z', \tau) = (2/(4\pi\alpha(t - \tau))^{3/2}) \exp(\,-((x - x')^2 + (y - y')^2 + (z - z')^2)/4\alpha(t - \tau))$ [49], α is the thermal diffusivity and k is the thermal conductivity.

The transient temperature can, therefore, be expressed in the form

$$T(x, y, z, t) = \left(\frac{2\alpha\eta P}{k z_p \pi r_b^2}\right) \int_{\tau=0}^{t} f(t - \tau)\, \mathrm{d}\tau. \tag{2.4}$$

This integral is straightforward to evaluate numerically using Gauss–Legendre quadrature. A detailed description of the function $f(t - \tau)$ and equation (2.4) are given in appendix A. The transient temperature is for the single layer. This could be considered appropriate because when another layer is built the scanned zone is already at a temperature close to that of the bulk.

(b) The inverse heat placement problem

Although the forward problem has a solution given explicitly by equation (2.4), which can easily and efficiently be evaluated numerically to give the temperature at any position or time for a given laser beam path and power, the solution of the *Inverse Heat Placement Problem* is significantly more challenging, for a number of reasons. We seek a laser power and beam path that leads to as uniform as possible a maximum temperature at each point on the surface $z = 0$. To study

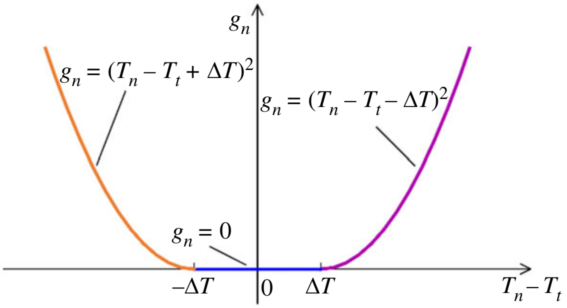

Figure 2. Schematics of g_n function. g_n is a defined function to calculate the deviation between the maximum temperature at the observation point n and the target value based on the consideration of a range of perturbation (ΔT).

the temperature distribution, observation points are distributed across the workpiece surface as squares. By adjusting the side length of squares between beam spot radius and hatching space, the observed points can be coarsely distributed in the area with steady temperature or densely distributed in the path corners. For raster paths, it is better to distribute observed points on the interval which has different distances to the path. While for curved paths, squared distribution can make observed points have different distances to the path naturally. At each of the observed points, the evolution of the temperature can be calculated from equation (2.4). This leads to the first challenge, which is to find this maximum at each observation point in a computationally efficient manner. We also need to define a suitable cost function whose minimum corresponds to the desired maximum temperature, along with constraints on the laser beam path and power that arise from practical considerations (for example, constraints based on maximum possible beam speed and acceleration). With the consideration of total fabrication time, during iteration, the average scanning speed is calculated after the cost function (with a small range of temperature variation as introduced in the following paragraph) is satisfied, and the solution with maximum average scanning speed is chosen. Finally, we must select a suitable iterative method to solve the *Inverse Heat Placement Problem* along with an initial guess of the optimal solution that satisfies the constraints.

In our modelling approach, we seek to control the maximum temperature generated by the moving laser. In order to try to create a homogeneous maximum temperature, and thereby obtain uniform microstructure properties, we define the cost function as the deviation from the target peak value (T_t). In practice, it is impossible to fix this maximum temperature at an exact value, and we allow temperature variation in a small range, ΔT (figure 2). We, therefore, define the cost function (C) to be

$$C = \frac{1}{N}\sum_{n}^{N} g_n, \tag{2.5}$$

where n is the index $(1, 2, 3, \dots, N)$ of the observation points which we place in a uniform mesh on the surface of the sample ($z = 0$); T_n is the maximum temperature of the nth observation point.

The simplest approach to obtain the maximum temperature is to search the whole temperature evolution at each observation point, but this is very time-consuming and inefficient. We assume that the temperature is maximal when the laser is close to the observation point. Locating the beam area where it is close to the observation point is more direct and efficient for finding the maximum temperature than global calculation and search. To make this clear, the temperature profiles in the time domain for the observation points are calculated based on equation (2.4).

Two cases of conventional laser predefined paths, i.e. raster and spiral, are chosen as examples to analyse the maximum distribution characteristics for a beam moving with a constant speed, i.e. the current way to conduct AM process. For each scenario, two generic cases could be taken into observation:

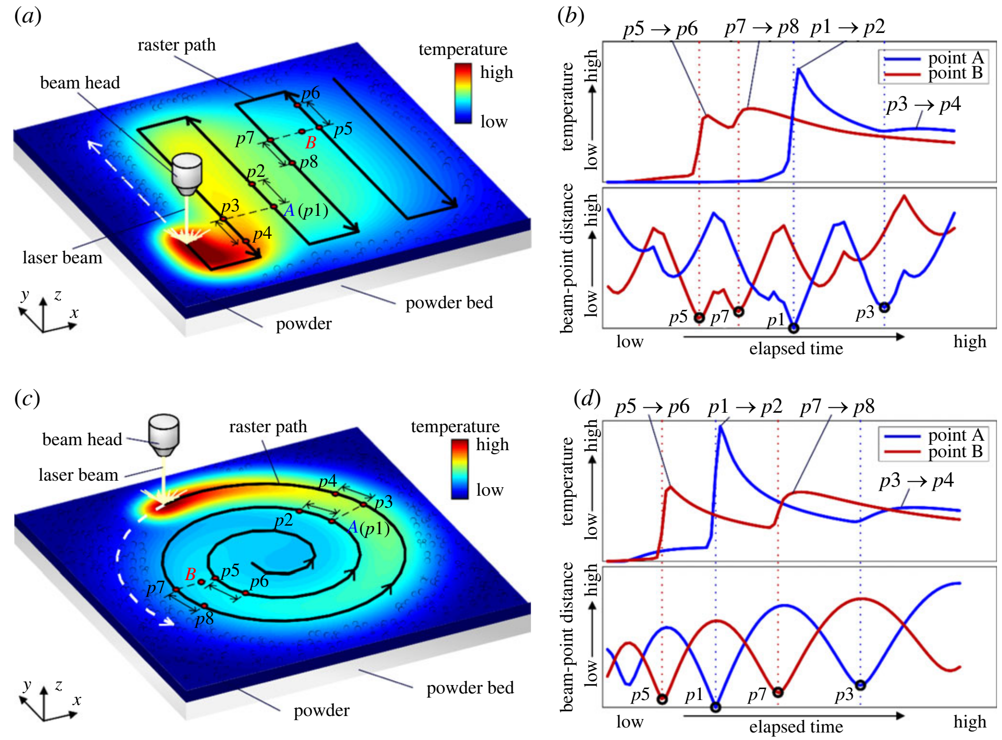

Figure 3. Temperature profiles in the time domain under raster (*a*,*b*) and spiral (*c*,*d*) paths. Point *A* is the observation point located at the beam path on the built part (*a*,*c*), and point *B* is another observation point located between two adjacent tracks on the built part (*a*,*c*). *p*1 and *p*3 are track approach points for point *A* (see the beam-point distance in (*b*,*d*)), *p*5 and *p*7 are track approach points for point *B* (see the beam-point distance in (*b*,*d*)). When the laser passes these approaching points, the local temperature peak value is reached (see the temperature in (*b*,*d*)).

- The observation point is located at the beam raster/spiral path (that is point *A* in figure 3*a*,*c*). In this case, the peak of the temperature profile (blue lines in the subfigure above figure 3*b*,*d*) is reached when the laser passes the approach points ($p1$ and $p3$) on the track where the observation point is located ($p1 \to p2$), or in the next track ($p3 \to p4$).
- The observation point is not at the beam raster/spiral path (that is point *B* in figure 3*a*,*c*). In this case, the peak (red lines in the subfigure above figure 3*b*,*d*) occurs at a similar location, but the approach points are in the preceding ($p5$) and subsequent ($p7$) tracks. This is a rationale for our use of a local search when the laser passes the approach points with a small range (i.e. $p5 \to p6$ and $p7 \to p8$).

A constant maximum temperature can be obtained by minimizing the cost function defined in equation (2.5) by controlling processing parameters. Several approaches are considered here to make comparisons, including (i) laser speed control; (ii) laser position control and (iii) combination control. In order to create a vector of control parameters, the predefined laser path is discretized into vectors with constant (arc) length ($\mathrm{d}l$). For the speed control (approach (i)), the time increment ($\mathrm{d}t$) for each vector is controlled to allow speed variations, while for the laser path control (approach (ii)), the perturbation relative to the vector nodes is used to express the control parameters as changes relative to the predefined path. The vectors of control parameters for the inverse model using each of these different approaches are, therefore,

$$\text{(i)}\quad \boldsymbol{u} = [\mathrm{d}t_1; \mathrm{d}t_2; \mathrm{d}t_3; \ldots; \mathrm{d}t_{N_b};], \tag{2.6}$$

$$\text{(ii)}\quad \boldsymbol{u} = [\mathrm{d}x_{b1}; \mathrm{d}x_{b2}; \mathrm{d}x_{b3}; \ldots; \mathrm{d}x_{bN_b}; \mathrm{d}y_{b1}; \mathrm{d}y_{b2}; \mathrm{d}y_{b3}; \ldots; \mathrm{d}y_{bN_b}] \tag{2.7}$$

and

$$\text{(iii)}\quad \boldsymbol{u} = [\mathrm{d}t_1; \mathrm{d}t_2; \mathrm{d}t_3; \ldots; \mathrm{d}t_{N_b}; \mathrm{d}x_{b1}; \mathrm{d}x_{b2}; \mathrm{d}x_{b3}; \ldots; \mathrm{d}x_{bN_b}; \mathrm{d}y_{b1}; \mathrm{d}y_{b2}; \mathrm{d}y_{b3}; \ldots; \mathrm{d}y_{bN_b};], \tag{2.8}$$

where N_b is the vector node number in the beam path.

We also need to define some constraints related to the dynamics of the laser. The laser beam scanning speed ($v_b = \mathrm{d}l/\mathrm{d}t$) should not exceed the allowed maximum ($v_{b\max}$), so the time increment ($\mathrm{d}t$) should satisfy:

$$\mathrm{d}t \geq \frac{\mathrm{d}l}{v_{b\max}}. \tag{2.9}$$

The laser beam scanning speed acceleration (a_b) should not exceed the allowed maximum ($a_{b\max}$) either, so that, using a simple approximation based on a constant acceleration,

$$-\frac{l^2 a_{b\max}}{v_{b\max}^3} \leq \mathrm{d}t_j - \mathrm{d}t_{j+1} \leq \frac{l^2 a_{b\max}}{v_{b\max}^3}. \tag{2.10}$$

The time increment should also be positive, so $\mathrm{d}t \geq 0$.

We used the sqp algorithm, which is built into the constrained minimization function *fmincon* in MATLAB, to solve this *Inverse Heat Placement Problem*. We provided this function with the gradient of the cost function with respect to the control parameters to accelerate the search process. The gradient of the cost function with respect to the control parameters given in equations (2.6)–(2.8) is discussed in appendix B. One key observation is that because this is a linear problem, and the control parameters only influence the function $q(\boldsymbol{x}, t)$ locally, the gradient can be calculated from a simple integral along a small section of the laser path, which is significantly more efficient than either perturbing the path and calculating the full temperature evolution or using an adjoint approach. In addition, the fact that the cost function depends upon the location of a maximum in T allows a significant simplification of the calculation.

3. Results and analysis

We wanted to experimentally verify the improvements offered by our inverse method to select the process parameters to obtain a uniform temperature distribution on the surface of the AM build structure when compared with existing methods. The scanning speed is fast and continuously changed on small incremental distances (comparable with radius of the laser beam, e.g. 50 µm) along the beam path. When the beam moves from one vector to another, the beam is powered on (i.e. no switch on-and-off actions). In our cases (equations (2.6)–(2.8)), the power is kept constant during scanning. However, the beam power and beam size can also be chosen as the controlling parameters in the Inverse Heat Placement Problem by using power-modulated continuous beams and alternative geometry-modulated continuous beams. Beam power is proportional to the temperature (as denoted in equation (2.4)) so the solution is much easier, but the beam size control needs to comprehensively consider the energy distribution over the powder bed and concentration in each beam spot. Similar to the scanning speed control, the variation of the beam power and beam size between vectors should be sharp but constant in each vector. Inconel 718 is one of the difficulty-to-machine materials. AM technologies are widely and successfully used for Inconel 718 to print the desired components in the aerospace field. We chose Inconel 718 as the printed material in the laser powder bed fusion system (as shown in table 1) and made comparison simulations with conventional approaches to demonstrate the significant improvements offered by our approach. Two laser paths were investigated as the predefined path, i.e. raster and spiral. These were used as follows:

- Using the conventional approach, i.e. a constant scanning speed of the beam.

Table 1. Inconel 718 property parameters and processing conditions.

parameter	value
density, ρ	8146 kg m^{-3}
thermal conductivity, k	$0.015 \times T + 11.002$ W (m K)$^{-1}$
specific heat capacity, c	1e3($0.0002 \times T + 0.4217$) J (kg K)$^{-1}$
heat absorption ratio, η	0.4
liquidus temperature, T_L	1337°C
laser spot size in radius, r_b	50 µm
laser power, P	280 W
hatch spacing, h_s	110 µm, 55 µm
constant speed, v_o	950 mm s^{-1}, 1200 mm s^{-1}

— Using variable scanning speeds and small deviations from the generic path (i.e. raster/spiral) that have been obtained using the solutions of our *Inverse Heat Placement Problem*.

The process parameters are shown in table 1. These are values that are usually employed in these circumstances [45,50]. In both cases, we compared the values of the maximum temperature on the AM built surface which, ultimately, proves the advantage of our approach. In laser powder bed AM processes, the powder, liquid and transition phases are all involved. The material properties of these phases are different, which will change the simulation result in absolute values. In this paper, we made a back-to-back comparison of the results obtained by the conventional (i.e. direct problem—trial and error) with our method (i.e. *Inverse Heat Placement Problem*). As such, these details on material aspects are not our focus as the approach we proposed here, and the comparison of the back-to-back results is independent of these.

(a) Raster path

The widely used raster path in AM was chosen as the predefined path. It is discretized into vectors with equal length (dl), and then the vector nodes (x_{br}, y_{br}) can be expressed as

$$\begin{cases} x_{br} = [0;0;0;\ldots;0;\mathrm{d}l;\mathrm{d}l;\mathrm{d}l;\ldots;\mathrm{d}l;2\mathrm{d}l;2\mathrm{d}l;2\mathrm{d}l;\ldots;2\mathrm{d}l;\ldots] \\ y_{br} = [0;\mathrm{d}l;2\mathrm{d}l;\ldots,(N_{bc}-1)\mathrm{d}l;\ (N_{bc}-1)\mathrm{d}l;\ (N_{bc}-2)\mathrm{d}l;(N_{bc}-3)\mathrm{d}l;\ldots,0;0;\mathrm{d}l;2\mathrm{d}l;\ldots,, \\ \qquad (N_{bc}-1)\mathrm{d}l;\ \ldots] \end{cases} \tag{3.1}$$

in which N_{bc} is the nodes number in the y-direction.

(b) Spiral path

The predefined spiral path is an Archimedean spiral, with vector nodes (x_{bs}, y_{bs}) given by

$$\begin{cases} x_{bs} = (a + b\theta)\cos\theta \\ y_{bs} = (a + b\theta)\sin\theta \end{cases}, \tag{3.2}$$

where θ is the radian angle of the spiral rotation; a is the radius when $\theta = 0$, which controls the spiral shape; b is the incremental radius per rotating degree, which controls the distance between tracks.

Here, θ is set as a vector $\theta_j (j = 1, \dots, N_b)$, given by

$$\theta_{j+1} = \frac{\left(-a + \sqrt{a^2 + 2b(\mathrm{d}l + a\theta_j + (b/2)\theta_j^2)}\right)}{b}, \tag{3.3}$$

$$a = \frac{h_s}{2} \tag{3.4}$$

and

$$b = \frac{h_s}{2\pi}, \tag{3.5}$$

where $\theta_1 = 0$ and h_s is the hatching space.

4. Analysis of simulation results

Based on the forward model, the maximum temperature in the conventional approach, i.e. Case I, where the beam follows the predefined raster path under a constant scanning speed is calculated. Figure 4*a* shows the non-uniform maximum temperature field following a raster, which is also lower than the desired value with an average error of 15.7% (see the dark blue solid line for Case I in figure 5). It shows a slightly increasing trend due to heat accumulation. The figures in the following discussion do not present the instantaneous temperature distribution, but the maximum values reached in all the points covering the printed part.

When our *Inverse Heat Placement Model* uses only the speed as the controlling factor (figure 4*b*), i.e. Case II, it does not change the path pattern but drags the maximum temperature to the nearby target value with an average error of 13.2% (see the purple solid line for Case II in figure 5). The optimized scanning speed (see the middle plot in figure 4*b*) shows a slight increase. This is consistent with the increase of maximum temperature with time using a constant beam speed.

When comparing Case III (optimized path) with Case II, this shows less perturbation in the maximum temperature map (figure 4*c* and light blue solid line in figure 5), but its deviation from the target value is in the same range as Case I with an average error of 10.0% (dark blue solid line in figure 5).

In Case IV, we optimized both beam speed on each element of the path and the path itself. This clearly shows a more uniform maximum temperature map (with an average error of 3.6%) than other cases (figure 4*d*) and the maximum temperature profile in the cross-section is around the target value (see green solid line in figure 5).

The vector length in the path is 55 µm and the distance between adjacent observation points is 54 µm. To avoid regularities in representing the local maximum temperature, the above uneven values are chosen for better uniformity.

Of course, our *Inverse Heat Placement Model* is not only applicable to the widely used raster path but also to other paths designed to align with the built shape. Here, as another example, a spiral case is chosen to compare with the conventional case. For the spiral path, a hatching space of 55 µm is chosen, and the overall maximum temperature is then higher than the raster path under the same laser power of 280 W, scanning speed of 950 mm s^{-1} (figure 6*a*). Based on previous findings, for this scenario, we have run simulations only for Case I (constant scanning speed and predefined path) and Case IV (variable scanning speed and optimized paths).

These trial-and-error approaches in simulation prove how tedious and imprecise is the conventional approach (i.e. using the solution of the direct problem) in selecting process parameters for laser powder bed AM, with very limited changes to reach the optimal solution.

By contrast, the solution of our *Inverse Heat Placement Problem* yields a much more uniform temperature distribution in a single run.

In this spiral path scenario, the temperature uniformity for Case I is improved but still is patterned and higher than the target value (i.e. 3000°C). As a comparison, the optimized spiral path, i.e. Case IV, with variant scanning speeds calculated from our *Inverse Heat Placement Model* gives a much more uniform maximum temperature map (figure 6*b*). Errors between the target value and the map under a constant speed of 950 mm s^{-1} (figure 7*a*, with an average error of

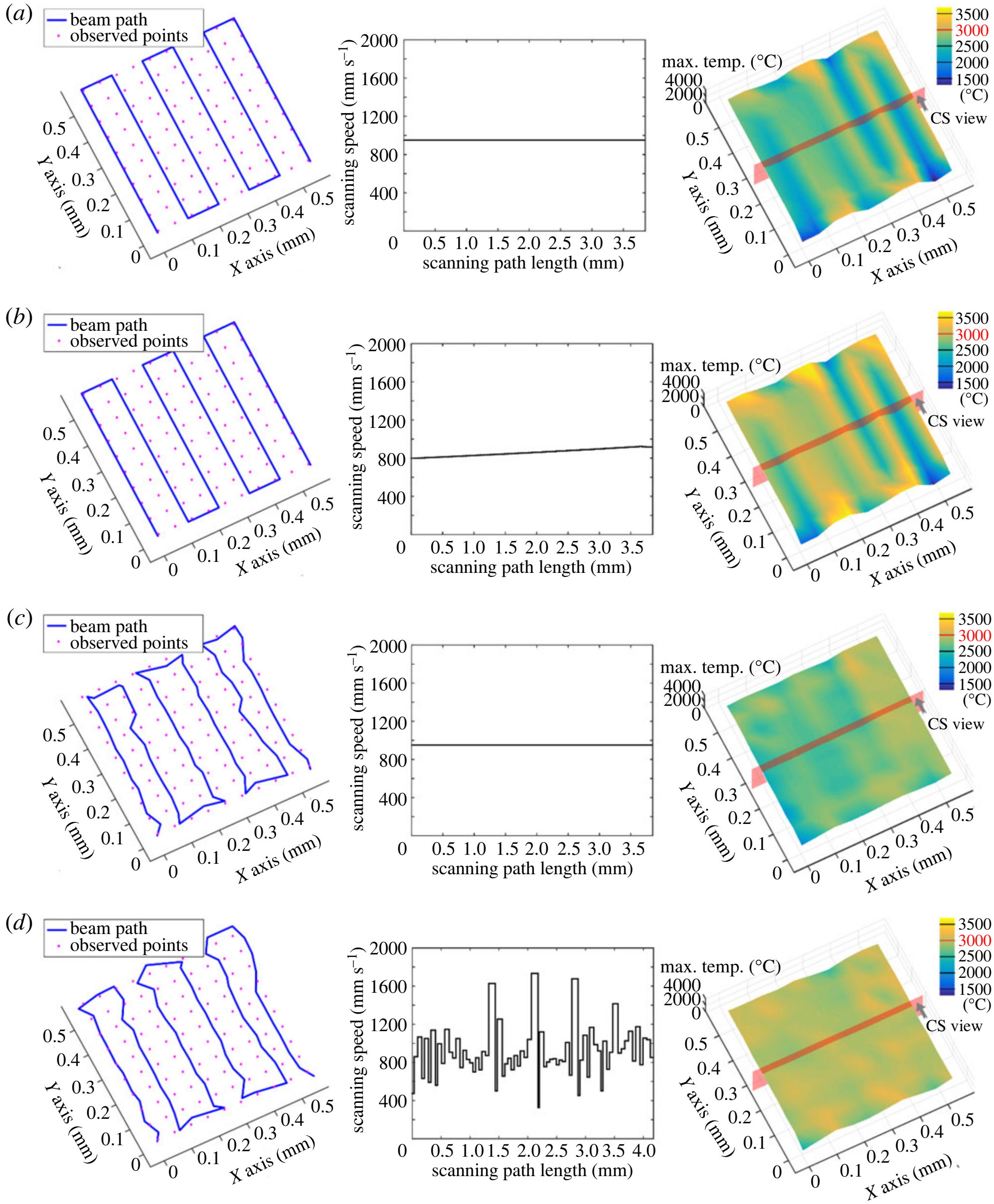

Figure 4. Local maximum temperature map under (*a*) Case I: predefined raster path and constant speed (950 mm s^{-1}), (*b*) Case II: predefined raster path and varied speeds, (*c*) Case III: optimized raster path and constant speed and (*d*) Case IV: optimized raster path and varied speeds.

15.9%) are much higher than the errors in the optimized case (figure 7*c*, with an average error of 3.2%). This is because the chosen constant speed is low and induces a long dwell time for melting the powder. Nevertheless, for the conventional approach, i.e. Case I, even when a higher constant value of the scanning speed (i.e. 1200 mm s^{-1}) is set, the uniformity is not improved (figure 7*b*, with an average error of 6.8%). The scanning speed of 1200 mm s^{-1} is around the average value of the optimized variant speeds. Lower and higher scanning speeds than this value cause larger errors.

We should note some issues associated with our approach that would benefit from more detailed analysis in the future. First, the optimized beam path and speed do show some

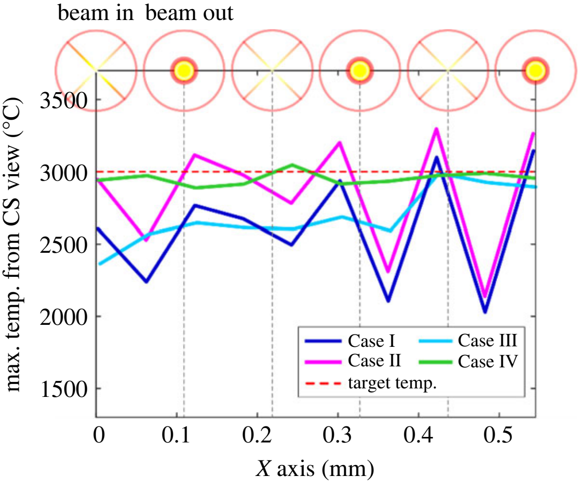

Figure 5. Profile of the maximum temperature map cross-sections.

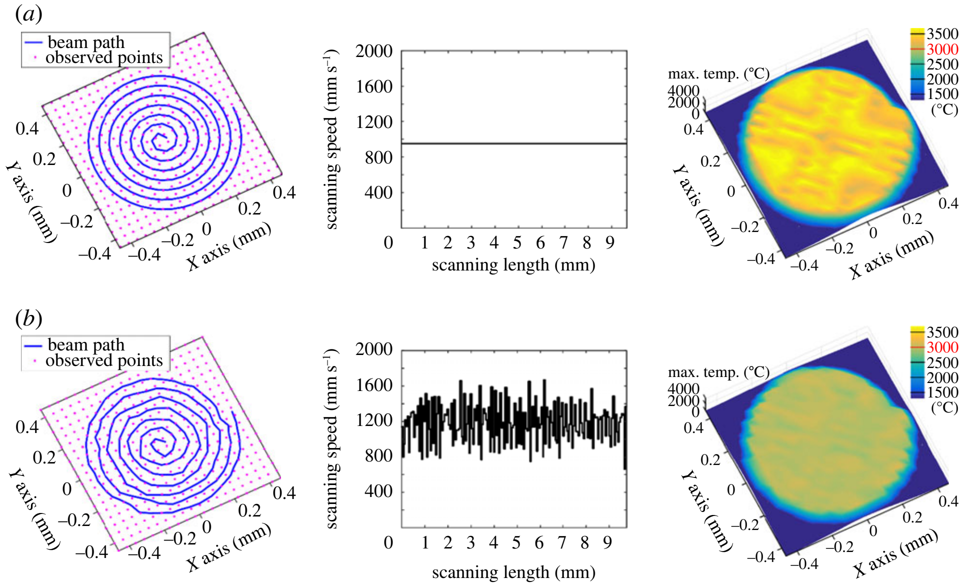

Figure 6. Local maximum temperature map under (*a*) a predefined spiral path and constant speed of 950 mm s^{-1} (Case I) and (*b*) an optimized spiral path and varied speeds (Case IV).

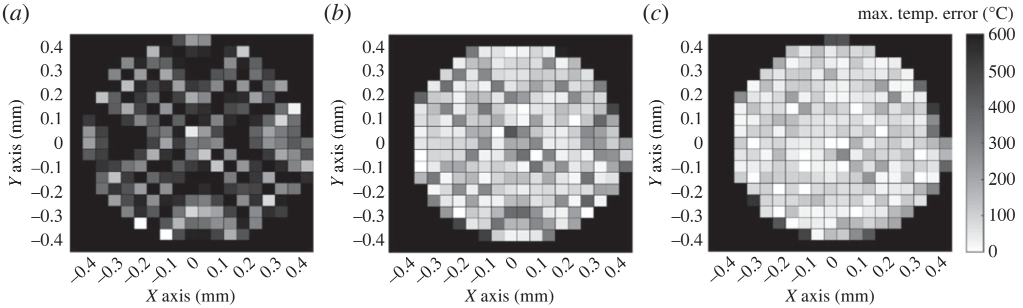

Figure 7. Errors between the target and the calculated temperature under (*a*) a predefined spiral path and constant speed of 950 mm s^{-1} (Case I), (*b*) a predefined spiral path and constant speed of 1200 mm s^{-1} (Case I) and (*c*) an optimized path and varied speeds (Case IV).

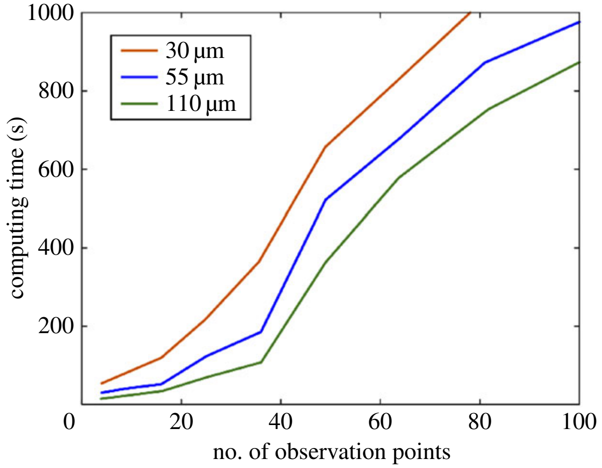

Figure 8. Computing time with vector length (30, 55 and 110 µm) and the number of observation points. This computing time is calculated under the same initial guess of control parameters in Case IV of the raster path.

dependence on the initial guess used, although the distance from the desired maximum temperature map remains similar. This is to be expected in a difficult global optimization problem with many local minima in the cost function. Second, the number of observation points chosen is a trade-off between computational speed and the accuracy of the solution. A large number of observation points allow greater control of the maximum temperature at the cost of longer computation times (figure 8). In a similar manner, choosing more points in the beam path (i.e. shorter vector length), and therefore more control parameters, allows more control of the beam (assuming this is carefully checked against the capabilities of the real beam control system) at the cost of longer computation times. The *Inverse Heat Placement Problem* approach is even more useful for creating small features or parts since these need to be divided into even smaller cells where the temperature must be controlled. For such small cells, the influence of the previous pass is more important, and hence it is more difficult to obtain a uniform maximum temperature distribution using the conventional, trial and error approach.

As well as the uniform maximum temperature, a maximum temperature map distributed as some predefined target patterns is not possible in the conventional case of a constant scanning speed. Using the approach outlined in this paper, we can achieve a good degree of control of the maximum temperature and try to achieve more complex patterns of maximum temperature. Here, a pattern composed of a rhombus, circle, square and triangle with small dimensions (less than 1 mm) is chosen as the target. Instead of setting the target temperature as a single value as in the uniform case, the target peak value is position-dependent. The target peak value on these shapes (rhombus, circle, square and triangle) is set as T_1(=2500°C) and on the remaining part of the surface at T_2(=1500°C). Our *Inverse Heat Placement Model* is able to compute the optimized scanning speed and beam path (figure 9*a*) to obtain the desired target pattern (figure 9*b*). This could be further used to control the processing parameters for obtaining other complex target values in three-dimensional printing of functionally graded materials.

5. Discussion and future work

The *Inverse Heat Placement Model* shows an obvious advantage in manipulating processing parameters for the target maximum temperature on the built surface. The consideration of laser scanning speed and beam path optimization is compared with the conventional case with constant scanning speed following the predefined raster and spiral path. It shows a better

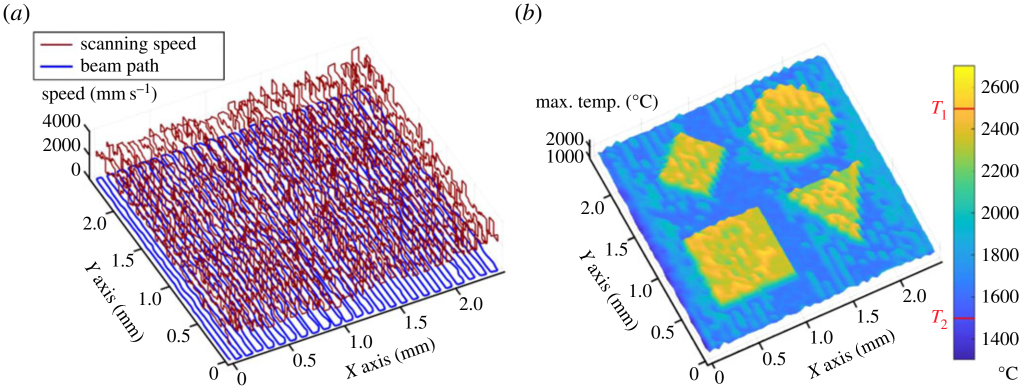

Figure 9. An example of raster beam path (variable speed as marked dark red solid line in (*a*) and optimized path as marked blue solid line in (*a*)) using our *Inverse Heat Placement Model* to generate rhombus, circle, square and triangle shapes (*b*) with a target surface temperature of T_1(=2500°C) and T_2(=1500°C).

uniformity and precision in obtaining the desired uniform maximum temperature. Our model further demonstrates its capability to obtain a complex target maximum temperature pattern by laser scanning speed and beam path control.

Here, our model only concerns heat placement factors, that is, laser scanning speed and beam path. In addition, laser power can be further considered in the inverse model by controlling energy input at the source. We note that in our modelling approach the beam speed remains constant along each vector but varies between vectors. The sharp changes between vectors are restricted by the allowable maximum acceleration of the laser movement. In future studies, we will consider a linearly varying speed on each vector to fit the speed variation allowed by the three-dimensional printing machine. The possibility of switching the laser on and off as part of its motion along the beam path preset in three-dimensional printing machines provides the convenience of simultaneous multi-sample printing. Nevertheless, it takes some time to reach the target power and scanning speed after turning on the laser switch again. This causes the real power to be lower than the nominal. It renders incomplete powder melting, especially when the vector has a short length. The needed adjusting time is related to the laser duty cycle. It would be better to keep the power on between vectors in such cases. When using a pulsed laser, dwell time is related to the pulse width and pulse position (corresponding to speed control in the case of the continuous wave laser). When using a power-modulated/geometry-modulated laser, the beam power and beam size can also be considered the controlling parameters in our method. The proposed method requires open-source controlling of the laser in terms of its power and speed so that the variation of speeds between vectors can be sharp for obtaining the desired temperature. It has been proved that the desired maximum temperature map (uniform map or target pattern) can be obtained by the heat placement control based on our algorithm. Further advancements can be made to link with thermal gradient and cooling rate control, i.e. thermal stress and microstructure, by inversely adjusting controlling parameters for the desired outcomes.

Data accessibility. Please find the codes in the Figshare link: A rational approach to beam path planning in additive manufacturing: the inverse heat placement problem (figshare.com). https://doi.org/10.6084/m9.figshare.21800747.v3.

Authors' contributions. Y.Y.: conceptualization, investigation, methodology, software, validation, visualization, writing—original draft; J.B.: conceptualization, investigation, methodology, software, supervision, writing—review and editing; D.A.: conceptualization, investigation, methodology, supervision, visualization, writing—review and editing; Z.L.: conceptualization, funding acquisition, investigation, supervision, visualization, writing—review and editing.

All authors gave final approval for publication and agreed to be held accountable for the work performed therein.

Conflict of interest declaration. We declare we have no competing interests.

Funding. The authors acknowledge the support from the University of Nottingham where the idea of this research was initiated. The authors would also like to thank Innovate UK for funding this research under the project THERMACH (74744). The University of Nottingham Propulsion Futures Beacon is also acknowledged. The first author gratefully appreciates the financial support from China Scholarship Council (CSC).

Appendix A

Substitution of the expression (equation (2.2)) for the heat source (q) and Green's function (G) on the right side of (equation (2.3)) gives

$$\begin{aligned}
&T(x,y,z,t)\\
&\quad=\frac{\alpha}{k}\int_{\tau=0}^{t}\int_{x'=-\infty}^{\infty}\int_{y'=-\infty}^{\infty}\int_{z'=-\infty}^{0}\frac{2}{(4\pi\alpha(t-\tau))^{3/2}}\\
&\qquad\times\exp\left(-\frac{(x-x')^2+(y-y')^2+(z-z')^2}{4\alpha(t-\tau)}\right)\frac{\eta P}{\pi r_b^2}\exp\left(-\frac{(x'-x_b(\tau))^2+(y'-y_b(\tau))^2}{r_b^2}\right)\frac{1}{z_p}\\
&\qquad\times\exp\left(\frac{z'}{z_p}\right)\mathrm{d}x'\mathrm{d}y'\mathrm{d}z'\mathrm{d}\tau\\
&\quad=\frac{2\alpha\eta P}{kz_p\pi r_b^2}\int_{\tau=0}^{t}\frac{1}{(4\pi\alpha(t-\tau))^{3/2}}\frac{4\pi\sqrt{\pi\alpha(t-\tau)}\left(1-\operatorname{erf}\left((z/2\sqrt{\alpha(t-\tau)})+(\sqrt{\alpha(t-\tau)}/z_p)\right)\right)}{1/(\alpha(t-\tau))+4/r_b^2}\\
&\qquad\times\exp\left(-\frac{(x-x_b(\tau))^2+(y-y_b(\tau))^2}{r_b^2+4\alpha(t-\tau)}\right)\exp\left(\frac{z}{z_p}+\frac{\alpha(t-\tau)}{z_p^2}\right)\mathrm{d}\tau\\
&\quad=\frac{2\alpha\eta P}{kz_p\pi r_b^2}\int_{\tau=0}^{t}f(t-\tau)\,\mathrm{d}\tau.
\end{aligned}\tag{A 1}$$

When $z=0$, then

$$\begin{aligned}
f(t-\tau)=&\frac{1}{(4\pi\alpha(t-\tau))^{3/2}}\frac{4\pi\sqrt{\pi\alpha(t-\tau)}\left(1-\operatorname{erf}\left(\sqrt{\alpha(t-\tau)}/z_p\right)\right)}{1/\alpha(t-\tau)+4/r_b^2}\\
&\times\exp\left(-\frac{(x-x_b(\tau))^2+(y-y_b(\tau))^2}{r_b^2+4\alpha(t-\tau)}\right)\exp\left(\frac{\alpha(t-\tau)}{z_p^2}\right),
\end{aligned}\tag{A 2}$$

in which $\exp(\alpha(t-\tau)/z_p^2)\rightarrow+\infty$ and $\left(1-\operatorname{erf}\left(\sqrt{\alpha(t-\tau)}/z_p\right)\right)\rightarrow 0$ as $(t-\tau)\rightarrow+\infty$. We, therefore, used an asymptotic expansion for sufficiently large values of $(t-\tau)$ so that

$$f(t-\tau)=\begin{cases}\dfrac{1}{2\alpha(t-\tau)}\left(1-\operatorname{erf}\left(\dfrac{\sqrt{\alpha(t-\tau)}}{z_p}\right)\right)\dfrac{1}{1/\alpha(t-\tau)+4/r_b^2}\\ \quad\times\exp\left(-\dfrac{(x-x_b(\tau))^2+(y-y_b(\tau))^2}{r_b^2+4\alpha(t-\tau)}+\dfrac{\alpha(t-\tau)}{z_p^2}\right), & t-\tau\le\dfrac{100z_p^2}{\alpha}\\ \dfrac{4\pi z_p}{(4\pi\alpha(t-\tau))^{3/2}}\dfrac{1}{1/\alpha(t-\tau)+4/r_b^2}\exp\left(-\dfrac{(x-x_b(\tau))^2+(y-y_b(\tau))^2}{r_b^2+4\alpha(t-\tau)}\right), & t-\tau>\dfrac{100z_p^2}{\alpha}\end{cases}\tag{A 3}$$

Appendix B

The gradient of the cost function with respect to the time increment is

$$\frac{\partial C}{\partial \mathrm{d}t_j} = \frac{1}{N}\sum_{n}^{N} \frac{\partial g_n}{\partial \mathrm{d}t_j}, \tag{B 1}$$

$$\frac{\partial g_n}{\partial \mathrm{d}t_j} = \begin{cases} 2(T_n - T_t - \Delta T)\dfrac{\partial T_n}{\partial \mathrm{d}t_j}, & T_n - T_t > \Delta T \\ 0, & |T_n - T_t| \le \Delta T \\ 2(T_n - T_t + \Delta T)\dfrac{\partial T_n}{\partial \mathrm{d}t_j}, & T_n - T_t < -\Delta T \end{cases} \tag{B 2}$$

and

$$\frac{\partial T_n}{\partial \mathrm{d}t_j} = \begin{cases} 0, & j > I_n + 1 \\ \dfrac{2\alpha q_0}{k z_p}\left(\dfrac{1}{l_{I_n+1}}\displaystyle\int_{s_{I_n+1}}^{s_n} f(t(s_n) - t(s))\mathrm{d}s + \dfrac{\mathrm{d}t_{I_n+1}}{l_{I_n+1}^2} \right. & \\ \qquad \left. \times \displaystyle\int_{s_{I_n+1}}^{s_n} \dfrac{\mathrm{d}f}{\mathrm{d}t}(t(s_n) - t(s))(s_n - s)\mathrm{d}s\right), & j = I_n + 1\,, \\ \dfrac{2\alpha q_0}{k z_p}\left(\dfrac{1}{l_j}\displaystyle\int_{s_j}^{s_{j+1}} f(t(s_n) - t(s))\mathrm{d}s + \dfrac{\mathrm{d}t_j}{l_j^2}\displaystyle\int_{s_j}^{s_{j+1}} \dfrac{\mathrm{d}f}{\mathrm{d}t}(t(s_n) - t(s))(s_{j+1} - s)\mathrm{d}s\right), & j < I_n + 1 \end{cases} \tag{B 3}$$

where s is the beam position in path length; s_n and $I_n + 1$ are the beam position and vector node number when the temperature at a particular point is maximum (T_n). Here, the temperature equation is considered as the beam moving arc length (s) function, and the speed in each vector is constant. Note that this involves integrals along the two adjacent vectors only, and not the full path, which makes this analytical approach very efficient. A key part of the derivation of this expression and those given below is that the temperature, by definition, is a local maximum at this time, so that the time-derivative is zero.

$$\text{Let} \begin{cases} A1 = \dfrac{1}{2\alpha(t-\tau)} \\ A2 = 1 - erf\left(\dfrac{\sqrt{\alpha(t-\tau)}}{z_p}\right) \\ A3 = \dfrac{1}{1/\alpha(t-\tau) + 4/r_b^2} \\ A4 = \exp\left(-\dfrac{(x - x_b(\tau))^2 + (y - y_b(\tau))^2}{r_b^2 + 4\alpha(t-\tau)} + \dfrac{\alpha(t-\tau)}{z_p^2}\right) \\ B1 = \dfrac{4\pi z_p}{(4\pi\alpha(t-\tau))^{3/2}} \\ B2 = A3 \\ B3 = \exp\left(-\dfrac{(x - x_b(\tau))^2 + (y - y_b(\tau))^2}{r_b^2 + 4\alpha(t-\tau)}\right) \end{cases}$$

$$
\text{then}\begin{cases}
\dfrac{\mathrm{d}A1}{\mathrm{d}t} = -\dfrac{1}{2\alpha(t-\tau)^2}\\[2ex]
\dfrac{\mathrm{d}A2}{\mathrm{d}t} = -\dfrac{1}{z_p}\sqrt{\dfrac{\alpha}{\pi(t-\tau)}}\exp\left(-\dfrac{\alpha(t-\tau)}{z_p^2}\right)\\[2ex]
\dfrac{\mathrm{d}A3}{\mathrm{d}t} = \dfrac{\alpha r_b^4}{\left(r_b^2+4\alpha(t-\tau)\right)^2}\\[2ex]
\dfrac{\mathrm{d}A4}{\mathrm{d}t} = A4 * \left(\dfrac{(x-x_b(\tau))^2+(y-y_b(\tau))^2}{\left(r_b^2+4\alpha(t-\tau)\right)^2} * 4\alpha + \dfrac{\alpha}{z_p^2}\right)\\[2ex]
\dfrac{\mathrm{d}B1}{\mathrm{d}t} = \dfrac{-24\pi^2\alpha z_p}{(4\pi\alpha(t-\tau))^{\frac{5}{2}}}\\[2ex]
\dfrac{\mathrm{d}B2}{\mathrm{d}t} = \dfrac{\mathrm{d}A3}{\mathrm{d}t}\\[2ex]
\dfrac{\mathrm{d}B3}{\mathrm{d}t} = B3 * \left(\dfrac{(x-x_b(\tau))^2+(y-y_b(\tau))^2}{\left(r_b^2+4\alpha(t-\tau)\right)^2} * 4\alpha\right)
\end{cases}
$$

We can then write

$$
\frac{\mathrm{d}f}{\mathrm{d}t} = \begin{cases}
\dfrac{\mathrm{d}A1}{\mathrm{d}t} * A2 * A3 * A4 + A1 * \dfrac{\mathrm{d}A2}{\mathrm{d}t} * A3 * A4 + A1 * A2 * \dfrac{\mathrm{d}A3}{\mathrm{d}t} * A4 & \\
\quad + A1 * A2 * A3 * \dfrac{\mathrm{d}A4}{\mathrm{d}t}, & t-\tau \le \dfrac{100z_p^2}{\alpha}\\[2ex]
\dfrac{\mathrm{d}B1}{\mathrm{d}t} * B2 * B3 + B1 * \dfrac{\mathrm{d}B2}{\mathrm{d}t} * B3 + B1 * B2 * \dfrac{\mathrm{d}B3}{\mathrm{d}t}, & t-\tau > \dfrac{100z_p^2}{\alpha}
\end{cases}. \tag{B 4}
$$

The gradient of the cost function to perturbations in x (or y) axis is

$$
\frac{\partial C}{\partial \mathrm{d}x_j} = \frac{1}{N}\sum_{n}^{N}\frac{\partial g_n}{\partial \mathrm{d}x_j}, \tag{B 5}
$$

$$
\frac{\partial g_n}{\partial \mathrm{d}x_j} = \begin{cases}
2(T_n - T_t - \Delta T)\dfrac{\partial T_n}{\partial \mathrm{d}x_j}, & T_n - T_t > \Delta T\\
0, & |T_n - T_t| \le \Delta T\\
2(T_n - T_t + \Delta T)\dfrac{\partial T_n}{\partial \mathrm{d}x_j}, & T_n - T_t < -\Delta T
\end{cases}, \tag{B 6}
$$

$$
\frac{\partial T_n}{\partial \mathrm{d}x_j} = \begin{cases}
0, & j > I_n + 1\\
\dfrac{2\alpha q_0}{k z_p}\int_{\tau=0}^{t}\dfrac{\partial f}{\partial \mathrm{d}x_{I_n+1}}\mathrm{d}\tau, & j = I_n + 1\\
\dfrac{2\alpha q_0}{k z_p}\int_{\tau=0}^{t}\dfrac{\partial f}{\partial \mathrm{d}x_j}\mathrm{d}\tau, & j < I_n + 1
\end{cases} \tag{B 7}
$$

$$\frac{\partial f}{\partial \mathrm{d}x}=\begin{cases}\dfrac{1}{2\alpha(t-\tau)}\left(1-\mathrm{erf}\left(\sqrt{\alpha(t-\tau)}/z_p\right)\right)\dfrac{1}{1/(\alpha(t-\tau))+4/r_b^2}\\ \quad\times\exp\left(-\dfrac{(x-x_b(\tau))^2+(y-y_b(\tau))^2}{r_b^2+4\alpha(t-\tau)}+\dfrac{\alpha(t-\tau)}{z_p^2}\right)*\dfrac{2(x-x_b(\tau))}{r_b^2+4\alpha(t-\tau)}, & t-\tau\le\dfrac{100z_p^2}{\alpha}\\ \dfrac{4\pi z_p}{(4\pi\alpha(t-\tau))^{3/2}}\dfrac{1}{(1/\alpha(t-\tau))+4/r_b^2}\\ \quad\times\exp\left(-\dfrac{(x-x_b(\tau))^2+(y-y_b(\tau))^2}{r_b^2+4\alpha(t-\tau)}\right)*\dfrac{2(x-x_b(\tau))}{r_b^2+4\alpha(t-\tau)}, & t-\tau>\dfrac{100z_p^2}{\alpha}\end{cases}. \tag{B 8}$$

References

1. Sanchez S, Smith P, Xu Z, Gaspard G, Hyde CJ, Wits WW, Ashcroft IA, Chen H, Clare AT. 2021 Powder bed fusion of nickel-based superalloys: a review. *Int. J. Mach. Tools Manuf.* **165**, 103729. (doi:10.1016/j.ijmachtools.2021.103729)
2. Tan C, Weng F, Sui S, Chew Y, Bi G. 2021 Progress and perspectives in laser additive manufacturing of key aeroengine materials. *Int. J. Mach. Tools Manuf.* **170**, 103804. (doi:10.1016/j.ijmachtools.2021.103804)
3. Koepf JA, Gotterbarm MR, Markl M, Körner C. 2018 3D multi-layer grain structure simulation of powder bed fusion additive manufacturing. *Acta Mater.* **152**, 119–126. (doi:10.1016/j.actamat.2018.04.030)
4. Wang R, Gu D, Lin K, Chen C, Ge Q, Li D. 2022 Multi-material additive manufacturing of a bio-inspired layered ceramic/metal structure: formation mechanisms and mechanical properties. *Int. J. Mach. Tools Manuf.* **175**, 103872. (doi:10.1016/j.ijmachtools.2022.103872)
5. Tan C, Chew Y, Weng F, Sui S, Ng FL, Liu T, Bi G. 2022 Laser aided additive manufacturing of spatially heterostructured steels. *Int. J. Mach. Tools Manuf.* **172**, 103817. (doi:10.1016/j.ijmachtools.2021.103817)
6. Kao A, Gan T, Tonry C, Krastins I, Pericleous K. 2020 Thermoelectric magnetohydrodynamic control of melt pool dynamics and microstructure evolution in additive manufacturing. *Phil. Trans. R Soc. A* **378**, 20190249. (doi:10.1098/rsta.2019.0249)
7. Zhao X, Iyer A, Promoppatum P, Yao S-C. 2017 Numerical modeling of the thermal behavior and residual stress in the direct metal laser sintering process of titanium alloy products. *Addit. Manuf.* **14**, 126–136. (doi:10.1016/j.addma.2016.10.005)
8. Sreejith P, Kannan K, Rajagopal KR. 2021 A thermodynamic framework for additive manufacturing, using amorphous polymers, capable of predicting residual stress, warpage and shrinkage. *Int. J. Eng. Sci.* **159**, 103412. (doi:10.1016/j.ijengsci.2020.103412)
9. Uddin SZ, Murr LE, Terrazas CA, Morton P, Roberson DA, Wicker RB. 2018 Processing and characterization of crack-free aluminum 6061 using high-temperature heating in laser powder bed fusion additive manufacturing. *Addit. Manuf.* **22**, 405–415. (doi:10.1016/j.addma.2018.05.047)
10. Acharya R, Sharon JA, Staroselsky A. 2017 Prediction of microstructure in laser powder bed fusion process. *Acta Mater.* **124**, 360–371. (doi:10.1016/j.actamat.2016.11.018)
11. Gu H, Wei C, Li L, Han Q, Setchi R, Ryan M, Li Q. 2020 Multi-physics modelling of molten pool development and track formation in multi-track, multi-layer and multi-material selective laser melting. *Int. J. Heat Mass Transfer* **151**, 119458. (doi:10.1016/j.ijheatmasstransfer.2020.119458)
12. Khorasani M, Ghasemi A, Leary M, O'Neil W, Gibson I, Cordova L, Rolfe B. 2021 Numerical and analytical investigation on meltpool temperature of laser-based powder bed fusion of IN718. *Int. J. Heat Mass Transfer* **177**, 121477. (doi:10.1016/j.ijheatmasstransfer.2021.121477)
13. Oliveira JP, LaLonde AD, Ma J. 2020 Processing parameters in laser powder bed fusion metal additive manufacturing. *Mater. Des.* **193**, 108762. (doi:10.1016/j.matdes.2020.108762)
14. Bayat M, Mohanty S, Hattel JH. 2019 A systematic investigation of the effects of process parameters on heat and fluid flow and metallurgical conditions during laser-based powder bed fusion of Ti6Al4V alloy. *Int. J. Heat Mass Transfer* **139**, 213–230. (doi:10.1016/j.ijheatmasstransfer.2019.05.017)

15. Criales LE, Arısoy YM, Lane B, Moylan S, Donmez A, Özel T. 2017 Laser powder bed fusion of nickel alloy 625: experimental investigations of effects of process parameters on melt pool size and shape with spatter analysis. *Int. J. Mach. Tools Manuf.* **121**, 22–36. (doi:10.1016/j.ijmachtools.2017.03.004)
16. Liu Y, Zhang J, Pang Z, Wu W. 2018 Investigation into the influence of laser energy input on selective laser melted thin-walled parts by response surface method. *Opt. Lasers Eng.* **103**, 34–45. (doi:10.1016/j.optlaseng.2017.11.011)
17. Gokcekaya O, Ishimoto T, Hibino S, Yasutomi J, Narushima T, Nakano T. 2021 Unique crystallographic texture formation in Inconel 718 by laser powder bed fusion and its effect on mechanical anisotropy. *Acta Mater.* **212**, 116876. (doi:10.1016/j.actamat.2021.116876)
18. Guo Q, Qu M, Escano LI, Hojjatzadeh SMH, Young Z, Fezzaa K, Chen L. 2022 Revealing melt flow instabilities in laser powder bed fusion additive manufacturing of aluminum alloy via in-situ high-speed X-ray imaging. *Int. J. Mach. Tools Manuf.* **175**, 103861. (doi:10.1016/j.ijmachtools.2022.103861)
19. Trapp J, Rubenchik AM, Guss G, Matthews MJ. 2017 In situ absorptivity measurements of metallic powders during laser powder-bed fusion additive manufacturing. *Appl. Mater. Today* **9**, 341–349. (doi:10.1016/j.apmt.2017.08.006)
20. Wolff SJ, Wang H, Gould B, Parab N, Wu Z, Zhao C, Greco A, Sun T. 2021 In situ X-ray imaging of pore formation mechanisms and dynamics in laser powder-blown directed energy deposition additive manufacturing. *Int. J. Mach. Tools Manuf.* **166**, 103743. (doi:10.1016/j.ijmachtools.2021.103743)
21. McCann R*et al.* 2021 In-situ sensing, process monitoring and machine control in Laser Powder Bed Fusion: a review. *Addit. Manuf.* **45**, 102058. (doi:10.1016/j.addma.2021.102058)
22. Nadammal N, Mishurova T, Fritsch T, Serrano-Munoz I, Kromm A, Haberland C, Portella PD, Bruno G. 2021 Critical role of scan strategies on the development of microstructure, texture, and residual stresses during laser powder bed fusion additive manufacturing. *Addit. Manuf.* **38**, 101792. (doi:10.1016/j.addma.2020.101792)
23. Catchpole-Smith S, Aboulkhair N, Parry L, Tuck C, Ashcroft IA, Clare A. 2017 Fractal scan strategies for selective laser melting of ‘unweldable’ nickel superalloys. *Addit. Manuf.* **15**, 113–122. (doi:10.1016/j.addma.2017.02.002)
24. Rashid R, Masood SH, Ruan D, Palanisamy S, Rahman Rashid RA, Brandt M. 2017 Effect of scan strategy on density and metallurgical properties of 17-4PH parts printed by Selective Laser Melting (SLM). *J. Mater. Process. Technol.* **249**, 502–511. (doi:10.1016/j.jmatprotec.2017.06.023)
25. Pham M-S, Dovgyy B, Hooper PA, Gourlay CM, Piglione A. 2020 The role of side-branching in microstructure development in laser powder-bed fusion. *Nat. Commun.* **11**, 749. (doi:10.1038/s41467-020-14453-3)
26. Zhang W, Tong M, Harrison NM. 2020 Scanning strategies effect on temperature, residual stress and deformation by multi-laser beam powder bed fusion manufacturing. *Addit. Manuf.* **36**, 101507. (doi:10.1016/j.addma.2020.101507)
27. Zhang B, Zhang S, Yang H, Peng D, Wang Y, Zhu H. 2022 Investigating the influence of the scanning rotation angle on the microstructure and properties of LPBFed CuCr0.8 alloy. *J. Manuf. Process.* **84**, 1150–1161. (doi:10.1016/j.jmapro.2022.10.073)
28. Zhang Z, Chu B, Wang L, Lu Z. 2019 Comprehensive effects of placement orientation and scanning angle on mechanical properties and behavior of 316L stainless steel based on the selective laser melting process. *J. Alloys Compd.* **791**, 166–175. (doi:10.1016/j.jallcom.2019.03.082)
29. Obadimu SO, Kasha A, Kourousis KI. 2022 Tensile performance and plastic anisotropy of material extrusion steel 316L: influence of primary manufacturing parameters. *Addit. Manuf.* **60**, 103297. (doi:10.1016/j.addma.2022.103297)
30. Cao L, Li J, Hu J, Liu H, Wu Y, Zhou Q. 2021 Optimization of surface roughness and dimensional accuracy in LPBF additive manufacturing. *Opt. Laser Technol.* **142**, 107246. (doi:10.1016/j.optlastec.2021.107246)
31. Wang C, Tan X, Liu E, Tor SB. 2018 Process parameter optimization and mechanical properties for additively manufactured stainless steel 316L parts by selective electron beam melting. *Mater. Des.* **147**, 157–166. (doi:10.1016/j.matdes.2018.03.035)
32. Wu CL, Zai W, Man HC. 2021 Additive manufacturing of ZK60 magnesium alloy by selective laser melting: parameter optimization, microstructure and biodegradability. *Mater. Today Commun.* **26**, 101922. (doi:10.1016/j.mtcomm.2020.101922)

33. Ren K, Chew Y, Fuh JYH, Zhang YF, Bi GJ. 2019 Thermo-mechanical analyses for optimized path planning in laser aided additive manufacturing processes. *Mater. Des.* **162**, 80–93. (doi:10.1016/j.matdes.2018.11.014)
34. Luo Z, Zhao Y. 2018 A survey of finite element analysis of temperature and thermal stress fields in powder bed fusion additive manufacturing. *Addit. Manuf.* **21**, 318–332. (doi:10.1016/j.addma.2018.03.022)
35. Lee K-H, Yun GJ. 2022 Design optimization of thermally conductive support structure for laser powder-bed fusion process with part-scale thermal history. *Addit. Manuf.* **51**, 102627. (doi:10.1016/j.addma.2022.102627)
36. Chen C, Xiao Z, Wang Y, Yang X, Zhu H. 2021 Prediction study on in-situ reduction of thermal stress using combined laser beams in laser powder bed fusion. *Addit. Manuf.* **47**, 102221. (doi:10.1016/j.addma.2021.102221)
37. Masiagutova E, Cabanettes F, Sova A, Cici M, Bidron G, Bertrand P. 2021 Side surface topography generation during laser powder bed fusion of AlSi10Mg. *Addit. Manuf.* **47**, 102230. (doi:10.1016/j.addma.2021.102230)
38. de Campos Carolo L, Ordoñez RE. 2022 A review on the influence of process variables on the surface roughness of Ti-6Al-4 V by electron beam powder bed fusion. *Addit. Manuf.* **59**, 103103. (doi:10.1016/j.addma.2022.103103)
39. Poncelet O, Marteleur M, van der Rest C, Rigo O, Adrien J, Dancette S, Jacques PJ, Simar A. 2021 Critical assessment of the impact of process parameters on vertical roughness and hardness of thin walls of AlSi10Mg processed by laser powder bed fusion. *Addit. Manuf.* **38**, 101801. (doi:10.1016/j.addma.2020.101801)
40. Farshidianfar MH, Khodabakhshi F, Khajepour A, Gerlich AP. 2021 Closed-loop control of microstructure and mechanical properties in additive manufacturing by directed energy deposition. *Mater. Sci. Eng. A* **803**, 140483. (doi:10.1016/j.msea.2020.140483)
41. Rezaeifar H, Elbestawi M. 2022 Porosity formation mitigation in laser powder bed fusion process using a control approach. *Opt. Laser Technol.* **147**, 107611. (doi:10.1016/j.optlastec.2021.107611)
42. Halsey W, Ferguson J, Plotkowski A, Dehoff R, Paquit V. 2020 Geometry-independent microstructure optimization for electron beam powder bed fusion additive manufacturing. *Addit. Manuf.* **35**, 101354. (doi:10.1016/j.addma.2020.101354)
43. Axinte D, Billingham J, Bilbao Guillerna A. 2017 New models for energy beam machining enable accurate generation of free forms. *Sci. Adv.* **3**, e1701201. (doi:10.1126/sciadv.1701201)
44. Bilbao-Guillerna A, Axinte DA, Billingham J, Cadot GBJ. 2017 Waterjet and laser etching: the nonlinear inverse problem. *R. Soc. Open Sci.* **4**, 161031. (doi:10.1098/rsos.161031)
45. Shang Z, Liao Z, Sarasua JA, Billingham J, Axinte D. 2019 On modelling of laser assisted machining: forward and inverse problems for heat placement control. *Int. J. Mach. Tools Manuf.* **138**, 36–50. (doi:10.1016/j.ijmachtools.2018.12.001)
46. Axinte D, Billingham J. 2019 Time-dependent manufacturing processes lead to a new class of inverse problems. *Proc. Natl Acad. Sci. USA* **116**, 5341–5343. (doi:10.1073/pnas.1900420116)
47. Raghavan N, Dehoff R, Pannala S, Simunovic S, Kirka M, Turner J, Carlson N, Babu SS. 2016 Numerical modeling of heat-transfer and the influence of process parameters on tailoring the grain morphology of IN718 in electron beam additive manufacturing. *Acta Mater.* **112**, 303–314. (doi:10.1016/j.actamat.2016.03.063)
48. Montero-Sistiaga ML, Godino-Martinez M, Boschmans K, Kruth J-P, Van Humbeeck J, Vanmeensel K. 2018 Microstructure evolution of 316L produced by HP-SLM (high power selective laser melting). *Addit. Manuf.* **23**, 402–410. (doi:10.1016/j.addma.2018.08.028)
49. Cole K, Beck J, Haji-Sheikh A, Litkouhi B. 2010 *Heat conduction using Greens functions*. Boca Raton, FL: CRC Press.
50. Liang X, Dong W, Chen Q, To AC. 2021 On incorporating scanning strategy effects into the modified inherent strain modeling framework for laser powder bed fusion. *Addit. Manuf.* **37**, 101648. (doi:10.1016/j.addma.2020.101648)